Biomaterials Translational

Meticulously engineered three-dimensional-printed scaffold with microarchitecture and controlled peptide release for enhanced bone regeneration

*Jin Yang, Kanwal Fatima, Xiaojun Zhou, Chuanglong He**

Key Words:
angiogenesis; bone regeneration; methacrylated gelatin; methacrylated silk fibroin; osteogenesis; PTH

From the Contents

ABSTRACT

The repair of large load-bearing bone defects requires superior mechanical strength, a feat that a single hydrogel scaffold cannot achieve. The objective is to seamlessly integrate optimal microarchitecture, mechanical robustness, vascularisation, and osteoinductive biological responses to effectively address these critical load-bearing bone defects. To confront this challenge, three-dimensional (3D) printing technology was employed to prepare a polycaprolactone (PCL)-based integrated scaffold. Within the voids of 3D printed PCL scaffold, a methacrylate gelatin (GelMA)/ methacrylated silk fibroin (SFMA) composite hydrogel incorporated with parathyroid hormone (PTH) peptide-loaded mesoporous silica nanoparticles (PTH@MSNs) was embedded, evolving into a porous PTH@MSNs/GelMA/SFMA/PCL (PM@GS/PCL) scaffold. The feasibility of fabricating this functional scaffold with a customised hierarchical structure was confirmed through meticulous chemical and physical characterisation. Compression testing unveiled an impressive strength of 17.81 ± 0.83 MPa for the composite scaffold. Additionally, in vitro angiogenesis potential of PM@GS/PCL scaffold was evaluated through Transwell and tube formation assays using human umbilical vein endothelium, revealing the superior cell migration and tube network formation. The alizarin red and alkaline phosphatase staining assays using bone marrow-derived mesenchymal stem cells clearly illustrated robust osteogenic differentiation properties within this scaffold. Furthermore, the bone repair potential of the scaffold was investigated on a rat femoral defect model using micro-computed tomography and histological examination, demonstrating enhanced osteogenic and angiogenic performance. This study presents a promising strategy for fabricating a microenvironment-matched composite scaffold for bone tissue engineering, providing a potential solution for effective bone defect repair.

http://doi.org/10.12336/biomatertransl.2024.01.007

How to cite this article:
Yang, J.; Fatima, K.; Zhou, X.; He, C. Meticulously engineered three-dimensional-printed scaffold with microarchitecture and controlled peptide release for enhanced bone regeneration. *Biomater Transl.* **2024**, *5*(1), 69-83.

Introduction

The healing of large segmental bone defects remains a complex and formidable medical challenge.[1, 2] These defects can have diverse origins such as trauma, tumour resections, infection, or congenital abnormalities.[3-5] It's imperative to repair large segmental bone defects to reinstate the structural integrity and functionality of the affected limb or region. Owing to ongoing advancements in orthopaedic technology, a plethora of techniques have emerged for crafting bone scaffolds that precisely fulfil distinct requirements. Such techniques encompass electrospinning,[6] solvent casting,[7] gas foaming,[8] freeze-drying,[9] and three-dimensional (3D) printing.[10] Among aforementioned methods, 3D printing, also referred to as additive manufacturing, has gained prominence.[11] 3D printing technology offers significant potential in bone tissue engineering because of its exceptional capabilities in crafting highly customised, intricate designs, enabling rapid prototyping, and fabricating multifunctional scaffolds that facilitate tissue regeneration and seamless integration.[12, 13] In 3D printing, various biomaterials, including polymers, bioceramics, metals, and composites, are utilised with the selection based on specific criteria for the intended use of 3D-printed

products.[14, 15] These criteria encompass the desired mechanical properties, biocompatibility, degradation rate, and the capacity to support cell growth thus promoting tissue regeneration.[16] Polycaprolactone (PCL) has been a frequently employed polymer with biodegradable and biocompatible properties in 3D printing for bone tissue engineering.[17-19] While PCL offers numerous advantages, it's essential to recognise that it lacks inherent bioactivity, potentially impeding early vascularisation and diminishing osteogenic activity in the context of bone repair.[20] Therefore, an applicable PCL-based bone repair material should overcome some limitations of conventional bone scaffolds and possess the ability to induce vascularisation and bone regeneration.

New blood vessel formation is pivotal for tissue growth, wound healing, and organ development.[21] Vascularisation is crucial for maintaining tissue health, supporting growth and development, healing injuries, and enabling various physiological processes to function correctly.[22] Researchers have widely recognised the critical role of angiogenesis in the intricate processes of bone repair and regeneration.[23-25] Blood vessels can offer provide cells with oxygen and essential nutrients, and also contribute to the deposition of vital extracellular matrix components.[26] Notably, vascular endothelial growth factor (VEGF) acts as a potent stimulator of vascularisation and is essential for processes of neo-angiogenesis.[27] VEGF also has the ability to accelerate bone regeneration by facilitating angiogenesis, osteogenesis, and chondrogenesis, which ultimately leads to the successful healing of bone injuries and fractures.[28] VEGF's short half-life is a notable consideration.[29] Excessive doses or uncontrolled administration can lead to pathological angiogenesis. To address these concerns, several studies have explored the use of functional peptides to induce angiogenesis as an alternative to growth factors. Parathyroid hormone (PTH) is a central hormone synthesised by the parathyroid glands, modulating calcium and phosphate levels in the body.[30] PTH(1–34), composed of 1–34 amino acid sequence of PTH, represents the active fragment governing PTH's bone remodelling activity.[31] By emulating the effects of naturally occurring PTH, PTH(1–34) effectively stimulates osteogenic differentiation of osteoblasts, thereby increasing bone mass.[32] PTH(1–34) was clinically approved by U.S. Food and Drug Administration for the treatment of osteoporosis in 2002 and as a topical pharmaceutical agent for addressing bone defects. Studies have confirmed PTH's pro-osteogenic, pro-osteoclastogenic, and proangiogenic effects during bone defect repair.[33-35] Therefore, the integration of PTH(1–34) within a customised scaffold offers a promising avenue for seamlessly integrating angiogenic and osteogenic functionality in bone repair.

3D printing technology presents a highly promising solution for bone tissue engineering by allowing the construction of biomimetic bone implants with precise structures and mechanical properties.[36, 37] In these 3D printed constructs, biomaterials and growth factors are co-printed together to form porous structures conducive to bone regeneration. In the present study, a composite scaffold for load-bearing bone repair was designed and fabricated using 3D printing technology (**Figure 1**). PTH(1–34)-loaded mesoporous silica nanoparticles (PTH@MSNs, denoted as PM) were first fabricated and added into GelMA/SFMA composite hydrogel (denoted as GS), and subsequently infused into the voids of 3D-printed PCL scaffold to form a PM@GS/PCL composite scaffold.[38] Then, the physicochemical characteristics of composite scaffolds were studied. The porous structure within the composite scaffold offered a fundamental condition for maintaining nutrients transport and facilitated cell migration and growth. Cellular experiments confirmed that the PM@GS/PCL scaffold enhanced the migration and recruitment of human umbilical vein endothelial cells (HUVECs). Moreover, the scaffold exhibited angiogenic and osteogenic activities as evidenced by the tube formation of HUVECs and mineralised matrix formation of bone marrow-derived mesenchymal stem cells (BMSCs). Our experimental illustrated the PM@GS/PCL scaffold's ability to promote bone regeneration after implantation. This provides a promising idea for constructing engineered implants to treat load-bearing bone defects.

Methods

Preparation of PM@GS/PCL scaffolds

Preparation of MSNs and PMs

The MSNs were synthesised according to a previously established method.[39] In a flask, 24 mL of hexadecyltrimethylammonium chloride (Sigma-Aldrich Trading Co., Ltd., Shanghai, China) and 0.18 g of triethanolamine (Sigma-Aldrich Trading Co., Ltd.) were dissolved in 36 mL of distilled water at 60°C with gentle stirring. Subsequently, 20 mL of tetraethyl orthosilicate (Sigma-Aldrich Trading Co., Ltd.) dissolved in cyclohexane (Sinopharm Chemical Reagent Co., Ltd., Shanghai, China) was added drop by drop. The solution was stirred continuously at 60°C for a time duration of 60 hours. Upon synthesis completion, the samples were harvested and centrifugated at 11,964 × *g* for 60 minutes and purified with ethanol (Sinopharm Chemical Reagent Co., Ltd.). The residual surfactant was eliminated by immersing the samples in a solution composed of ethanol and NaCl at 80°C for 12 hours. Following that, surfactant-free MSNs were obtained through the second round of centrifugation, and the resulting freeze-dried powder was employed for further experimentation. The fluorescein isothiocyanate-labelled MSNs were also prepared according to the protocol.[39]

To load PTH(1–34) (hereafter referred to as PTH), 1 mg of PTH (Medchem Express, Shanghai, China) was added into 10 mL of phosphate-buffered saline (PBS; Beyotime Institute of

Shanghai Engineering Research Center of Nano-Biomaterials and Regenerative Medicine; College of Biological Science and Medical Engineering, Donghua University, Shanghai, China

***Corresponding author:** Chuanglong He, hcl@dhu.edu.cn.

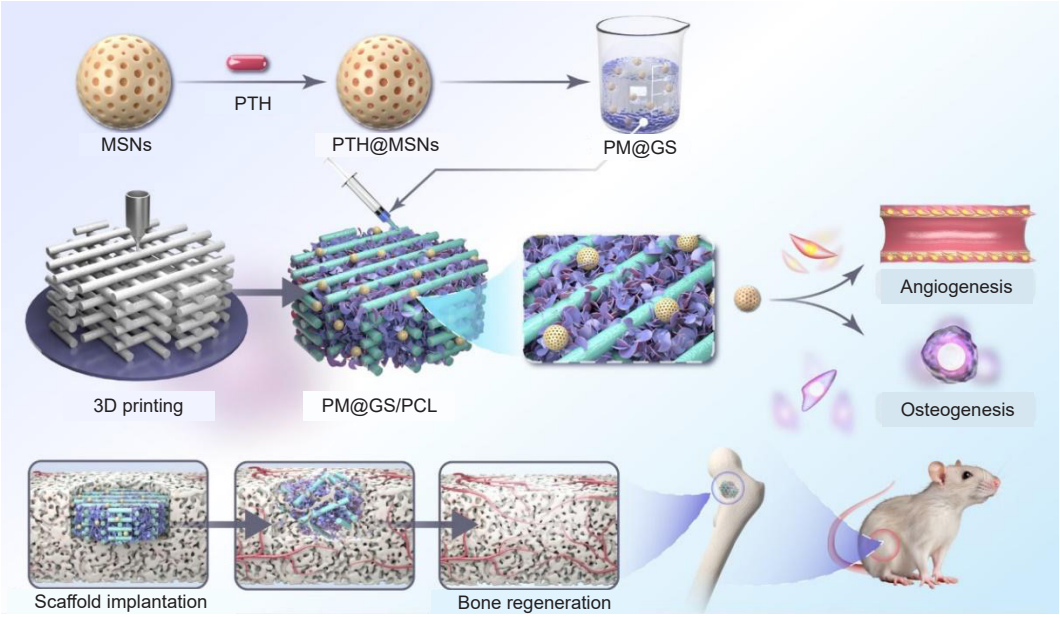

Figure 1. Schematic illustration of the construction of PM@GS/PCL composite scaffold and the process of promoting bone regeneration in a rat femoral defect model. 3D: three-dimensional; GelMA: methacrylate gelatin; MSNs: mesoporous silica nanoparticles; PCL: polycaprolactone; PM: PTH@MSNs; PM@GS/PCL: PTH@MSNs/GelMA/SFMA/PCL; PM@GS: PTH@MSNs/GelMA/SFMA; PTH: parathyroid hormone (1–34); PTH@MSNs: PTH-loaded MSNs; SFMA: methacrylated silk fibroin.

Biotechnology, Shanghai, China) to obtain a PTH solution. Following this, 0.1 g of MSNs was mixed with the PTH solution and stirred for 24 hours. The resulting products were obtained via centrifugation, and PTH concentration in the supernatant was determined using a PTH enzyme linked immunosorbent assay kit (Medchem Express). The loading content of PTH was calculated from the measured result.

Preparation of PM@GS and PM@GS/PCL scaffolds

GelMA and SFMA were synthesised as described previously.[40] GelMA and SFMA were separately dissolved in deionised water to get the solution and maintained at 40°C for subsequent use. Then, GelMA solution (10% w/v) and SFMA solution (20% w/v) were mixed in equal proportions, and 0.5% (w/v) lithium phenyl-2,4,6-trimethylbenzoylphosphinate (Sigma-Aldrich Trading Co., Ltd.) was gently added under stirring, taking care not to expose the mixture to light. This yielded a GelMA/SFMA solution, which remains in a liquid state at low temperatures (20°C) and can be crosslinked using visible light at 405 nm. The MSNs and PM nanoparticles were incorporated into the GelMA/SFMA hydrogel precursor to produce M@GS and PM@GS scaffolds.

PCL scaffolds were fabricated using a 3D printer (MAM-II FreeForm Fabrication System, Fochif Mechatronics Technology Co. Ltd., Shanghai, China). Uniform PCL spherical particles (average Mn ~45,000; Sigma-Aldrich Trading Co., Ltd.) were loaded into a stainless-steel barrel, heated to 70°C for 1 hour, and extruded at 70°C through a nozzle (0.33 ± 0.02 mm) at a constant extrusion speed of 0.002 mm/s using a screw mechanism. The nozzle moved at a speed of 6 mm/s during printing when using the designed model prepared by CAD software (version 2021; Autodesk, San Francisco,CA, USA). The distance between the microfilaments was controlled at 600 μm, and the scaffold was constructed by depositing filaments with a step angle of 90° and a thickness of 0.33 mm between successive layers. The injectable GelMA/SFMA hydrogel, M@GS hydrogel and PM@GS hydrogel were prepared and injected into the voids of the PCL scaffolds. The composites were maintained at 4°C for 1 hour and subsequently crosslinked using visible light. Finally, the GS/PCL, M@GS/PCL and PM@GS/PCL scaffolds were obtained and subjected to freeze-drying for 48 hours.

Characterisation of MSNs and scaffolds

The morphologies of MSNs and various scaffolds were observed through a scanning electron microscope (S-4800, Hitachi, Japan), and the microstructure of MSNs was examined using a transmission electron microscope (2100, JEM, Tokyo, Japan). Attenuated total reflectance-Fourier transform infrared spectroscopy was conducted on a Nicolet 6700 spectrometer (Thermo Fisher, Walyham, MA, USA). The particle size of MSNs was measured with dynamic/static laser scattering (DLS) equipment (BI-200SM, Brookhaven, New York, USA). The surface area and pore size of MSNs were calculated using Brunauer Emmett Teller and Barrett-Joyner-Halenda methods by nitrogen adsorption-desorption measurement on a Micromeritics Tristar II analyzer (Micromeritics, V-Sorb 2800P, Norcross, GA, USA).[39] The zeta potential of nanoparticles was detected using a Zetasizer Nano instrument (ZS, Malvern, Worcestershire, UK). The weight loss of MSNs and various scaffolds was monitored via thermogravimetric

analysis employing a thermogravimetric analyser (TG209F1, Netzsch, Selb, Germany) in a nitrogen atmosphere with a heating rate of 10°C/min and a peak of 800°C. The wettability of samples was studied by measuring the static water contact angles at room temperature. For compression testing, PCL and GS/PCL scaffolds were subjected to compression testing using a universal test system (CMT4202, Jiehu, Shanghai, China). The samples were compressed to a speed of 1 mm/min, and the compressive strength was determined by analysing the stress-strain curve. Six specimens were used in each test.

In vitro investigations

In vitro PTH release kinetics

To evaluate *in vitro* drug release, PTH was released from PM and PM@GS/PCL in PBS (pH 7.4). Specifically, 1 mg of PM and 30 mg of PM@GS/PCL, both containing PTH, were placed in centrifuge tubes containing 2.0 mL of PBS. These tubes were then shaken in a thermostatic shaker at 37°C with a speed of 100 r/min. At various time points, the medium was removed and replaced with the same volume of fresh medium. The amount of released PTH were quantified using a PTH enzyme-linked immunosorbent assay kit. All measurements were performed in triplicate.

Animal procedures and cell culture methods

All animal procedures adhered to local animal welfare laws and guidelines, as approved by the Animal Ethics Committee of Donghua University (No. DHUEC-NSFC-2022-27, on March 1, 2022). Sprague-Dawley rats (4-week-old, male, ~160 g, specific-pathogen-free grade, Shanghai SLAC Laboratory Animal Co. Ltd., Shanghai, China, license No. SCXK (Hu) 2022-0004) were euthanised by cervical dislocation, and their femurs and tibias were aseptically removed. Bone marrow was collected, and BMSCs were isolated and cultured in Dulbecco's modified Eagle medium/nutrient mixture F-12 (Gibco Life Technologies Co., Ltd.). The cell culture medium was changed every 2 days.

HUVECs sourced from the Orthopaedics Research Institute of Zhejiang University (ordered from Cell Bank of the Chinese Academy of Sciences, Shanghai, China) were cultured in RPMI-1640 medium (Gibco Life Technologies Co., Ltd.).

Cell proliferation study

In this study, cell proliferation of BMSCs on the scaffold was analysed using a cell counting kit-8 assay (Beyotime Institute of Biotechnology). Sterilised PCL, GS/PCL and PM@GS/PCL scaffolds were placed in 48-well plates and seeded with BMSCs (2×10^4 cells per well). After culturing for 1, 3, and 5 days, the medium was removed, and the scaffolds were washed with PBS. Cell counting kit-8 working solution was added to each well and incubated for 60 minutes. After incubation, the supernatant was collected and transferred to 96-well culture plates, and the absorbance was measured at 450 nm using a microplate reader (Multiskan GO, Thermo, Waltham, MA, USA). For visual observation of cell proliferation, BMSCs on the scaffold surface were stained with Calcein-AM/PI (Beyotime Institute of Biotechnology), and observed and photographed using an inverted fluorescence microscope (DMi8, Leica, Germany) on days 1, 3, and 5. The internalisation of MSNs within BMSCs was assessed using a confocal laser scanning microscope (LSM 700, Carl-Zeiss, Germany). After the cells were cultured with fluorescein isothiocyanate-labelled MSNs or MSNs for 48 hours, Alexa Fluor 568 phalloidin (red) and 4′,6-diamidino-2-phenylindole (blue) were used to stain the cells and then the fluorescence images were captured.

Transwell migration assay

HUVECs migration was assessed using a Transwell system (Corning Costar, Cambridge, MA, USA) with an 8 μm polycarbonate filter.[41] Sterilised PCL, GS/PCL and M@GS/PCL, and PM@GS/PCL scaffolds were placed in the lower chamber of Transwell, followed by addition of 600 μL of medium. Then 2×10^4 cells were seeded into the upper chamber. After incubation for 24 hours, cells on the lower surface of the membrane were fixed with 4% paraformaldehyde for 30 minutes, and stained with 1% crystal violet for 10 minutes.

In vitro assessment of angiogenic potential for PM@GS/PCL scaffolds

To assess the angiogenic potential of the PM@GS/PCL scaffold *in vitro*, we performed a Matrigel-based tube formation assay using HUVECs. Scaffolds with a 10 mm-diameter were placed in the 24-well plate ($n = 3$) and incubated with RPMI-1640 culture medium (fetal bovine serum-free medium) for 24 hours to obtain the extracellular fluid. HUVECs were grown on Matrigel containing the scaffold extract solution. In brief, Matrigel (Corning, Corning, NY, USA) was fixed on 48-well plates with a volume of 100 μL per well and incubated at 37°C for 30 minutes. HUVECs (2×10^4 cells/well) were then seeded on the Matrigel with the extract solution. After 6 and 24 hours of culture, the formation of tubular network was observed and imaged using fluorescence microscope. Several parameters (including total length, number of junctions, number of meshes, and total mesh area) in high-power field were quantified using ImageJ software (version 1.48, National Institute of Health, Bethesda, MD, USA).[42]

Evaluation of alkaline phosphatase activity

BMSCs (1×10^5 cells) were seeded in an osteoinductive medium consisting of 50 μg/mL ascorbic acid, 10 mM β-glycerophosphate, and 100 nM dexamethasone, and supplemented with an equal volume of extract solution. After culturing for 7 and 14 days, cells were washed with PBS and lysed using RIPA lysis solution (Beyotime Institute of Biotechnology). The supernatant was collected following centrifugation. Alkaline phosphatase (ALP) activity was determined using an ALP detection kit (Beyotime Institute of Biotechnology), and total protein content was assessed using a BCA protein detection kit (Beyotime Institute of Biotechnology). ALP activity in each sample was calculated according to the manufacturer's instructions. After 7 and 14 days of culture, the cells were treated with ALP staining and imaged using a microscope.

Alizarin red S staining

The PM@GS/PCL scaffold's capacity to stimulate the formation of mineralised nodules in BMSCs was assessed using an Alizarin red S (ARS) staining. Cells were cultured in an osteoinductive medium containing the extract liquid for 14 and 21 days. After fixing with 4% paraformaldehyde for 20 minutes, the cells were stained with a 2% ARS solution (Beyotime Institute of Biotechnology). After a 30-minute incubation at room temperature, excess ARS was discarded and washed with distilled water. Images of calcium nodules were captured using a digital camera and a microscope. To quantify the mineral formation, each sample was incubated with 10% acetic acid for overnight. The collected solution was then centrifuged to obtain a supernatant, which was subsequently mixed with 10% $NH_3 \cdot H_2O$. Finally, 100 μL of the supernatant was transferred to a new plate. The absorbance was measured at 405 nm using a microplate reader.

Gene expression analysis

To assess the extent of osteogenic differentiation in BMSCs and angiogenic capacity in HUVECs cultured on each scaffold, real-time polymerase chain reaction (RT-PCR) assay was performed. Initially, BMSCs were seeded on different scaffolds in six-well plates for 1 day. Subsequently, the medium was changed with osteoinductive medium and cultured for 7 and 14 days. HUVECs were seeded on different scaffolds with RPMI-1640 medium for 48 hours. Total cellular RNA was harvested from cell pellets using Trizol reagent (Invitrogen, USA) and converted into complementary DNA following the standard protocol. The quantification of complementary DNA was conducted using the SYBR Green qPCR Master Mix (TaKaRa, Kyoto, Japan) on an RT-PCR system (Applied Biosystems 7500, USA). RT-PCR was employed to test the expression of osteogenesis-related markers, including runt-related transcription factor 2 (*Runx2*), osteocalcin (*OCN*), and osteopontin (*OPN*). The mRNA expression of *VEGF* and platelet endothelial cell adhesion molecule-1 (*CD31*) in HUVECs was analysed as markers for angiogenesis, with glyceraldehyde-3-phosphate dehydrogenase (*GAPDH*) gene serving as a reference. The conditions of RT-PCR were used as follows: initial denaturation at 95°C for 2 minutes, 40 cycles of amplification at 95°C for 15 seconds and 62°C for 32 seconds. The primer sequences are shown **Additional Table 1**.

Evaluation of bone defect repair

To evaluate the efficacy of various scaffold materials in bone repair, the rat femoral condyle defect model was established. The Sprague-Dawley rats (8-week-old, male, ~200 g, specific-pathogen-free grade, Shanghai SLAC Laboratory Animal Co. Ltd.) were randomky categorised into four groups (n = 6): PCL, GS/PCL, M@GS/PCL, and PM@GS/PCL groups. Rats were intraperitoneally anaesthetised with 40 mg/kg pentobarbital sodium. Circular full-thickness defects, with a diameter of 3 mm, were surgically created on the femoral condyle. Subsequently, cylindrical scaffolds (diameter: 3 mm, height: 3 mm) from the four groups were implanted into the defect sites. Following 4 and 8 weeks of implantation, the rats were humanely euthanised, and their femoral condyles were collected.

Bone formation within the defect area was evaluated utilizing a micro-computed tomography (CT) scanner (SkyScan 1176, Bruker). The ratio of new bone volume to total volume (BV/TV), bone mineral density (BMD) and trabecular number (Tb.N) were analysed using SkyScan CT analyser (software version 1.9.1; SkyScan, Belgium).

Bone tissue of femoral condyle embedded in paraffin was sectioned into 5 μm thick slices for haematoxylin and eosin staining and Masson's trichrome staining as the guidelines provided by the manufacturer (Servicebio, Wuhan, China).

For immunofluorescence analysis, vascular network around the newly formed bone was assessed by staining for CD31 (1:200, Servicebio, Cat# GB11063) following the manufacturer's instructions. Additionally, osteogenic activity around the new bone tissue was assessed using antibodies against OCN (1:100, Servicebio, Cat# GB11233) and OPN (1:500, Servicebio, Cat# GB11500) using the manufacturer's instructions. 4′,6-Diamidino-2-phenylindole (Servicebio, Cat# G1012) was used for nuclear staining according to the manufacturer's instructions. Briefly, each slice was incubated with 3% bovine albumin for 30 minutes and the primary antibodies for overnight at 4°C. Then the secondary antibodies (Cy3 conjugated goat anti-rabbit IgG (H + L), 1:300, Servicebio, Cat# GB21303) were incubated at room temperature for 60 minutes and rinsed with 0.01 M PBS for 5 minutes. The fluorescence signal intensity was quantified using ImageJ software.

Statistical analysis

All data are presented as the mean ± standard deviation (SD) and were analysed using GraphPad Prism 8.0.2 (GraphPad Software, Boston, MA, USA, www.graphpad.com). The statistical analysis was performed using one-way analysis of variance followed by Tukey's *post hoc* test. Statistically significant differences between groups were indicated by $P < 0.05$.

Results

Preparation and characterisation of MSNs

The MSNs synthesised via the hydrothermal method displayed a consistent size distribution and an organised arrangement, as depicted from the transmission electron microscopy and scanning electron microscopy results in **Figure 2A**, and **B**. The nanoparticles of MSNs exhibited a homogeneous spherical shape. Nitrogen adsorption-desorption results (**Figure 2C**) exhibited a classical type IV isotherm for the MSNs, confirming their mesoporous nature. The specific surface area was measured to be 269.3 m^2/g by Brunauer-Emmett-Teller method, and the pore size was calculated to be 7.2 nm by Barrett-Joyner-Halenda method. DLS analysis indicated that the hydrodynamic size of the MSNs and PM nanoparticles was 168.2 nm and 177.8 nm, respectively (**Figure 2D**). The average zeta potential of PTH, MSNs, MSNs-NH_2, and PM-NH_2 was observed to be –11.8, –8.6, +8.7, and +3.0 mV, respectively (**Figure 2E**), respectively, due to the presence of carboxyl groups in PTH. DLS and zeta potential analyses confirmed the successful loading of PTH into the MSNs.

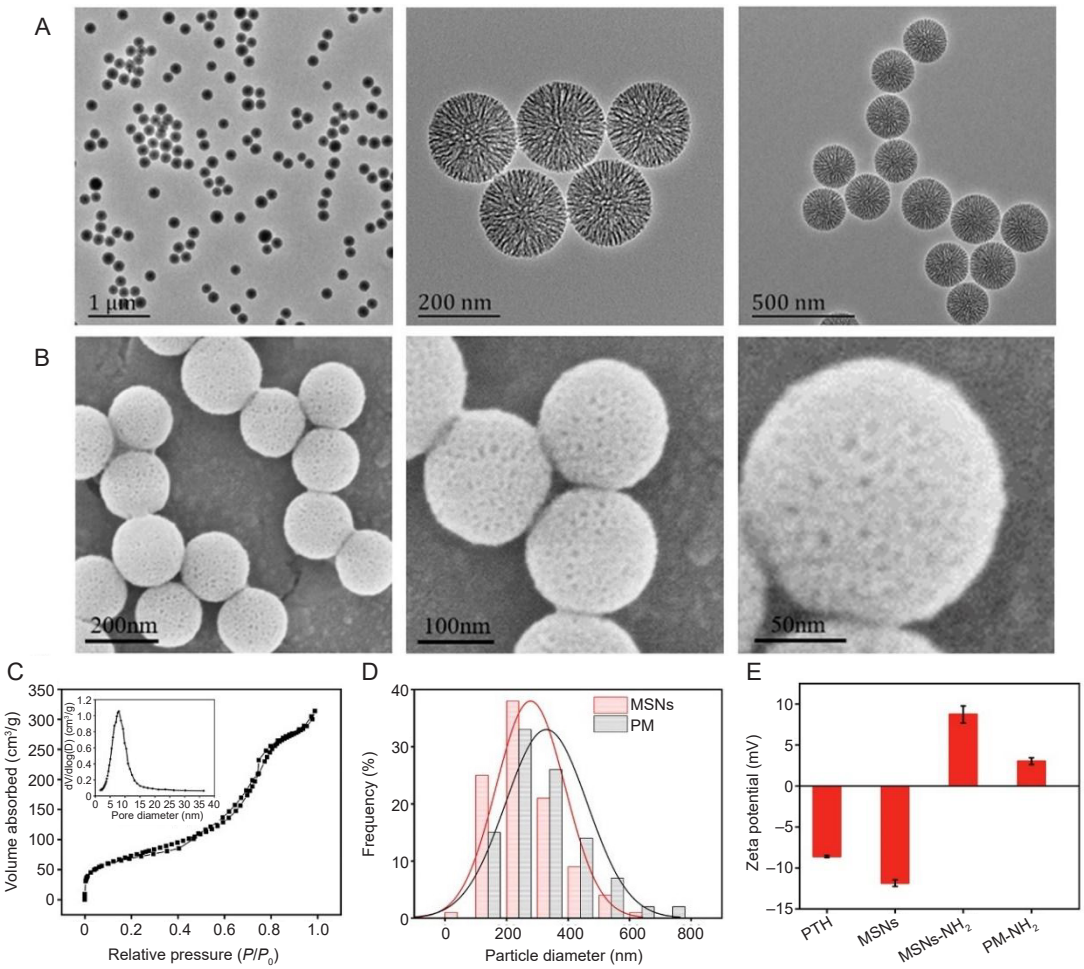

Figure 2. Characterisation of MSNs and PMs. (A) TEM images of MSNs at various magnifications. Scale bars: 1 μm (left), 200 nm (middle) and 500 nm (right). (B) SEM images of MSNs at various magnifications. The nanoparticles of MSNs exhibited a homogeneous spherical shape with mesoporous structure. Scale bars: 200 nm (left), 100 nm (middle) and 50 nm (right). (C) The nitrogen absorption-desorption isotherm curves of MSNs and the pore size distribution inside. (D) Size distribution of MSNs and PMs. (E) Zeta potential results of different samples. MSNs: mesoporous silica nanoparticles; *P*: the equilibrium adsorption pressure of the gas; P_0: the saturated vapour pressure of the gas at the adsorption temperature; PM: PTH@MSNs; PTH: parathyroid hormone (1–34); SEM: scanning electron microscope; TEM: transmission electron microscope.

Fabrication and characterisation of composite scaffolds

From scanning electron microscope images of different scaffolds (**Figure 3A**), PCL scaffolds have macroporous structure, while GS/PCL and M@GS/PCL scaffolds were obviously filled with GelMA/SFMA hydrogel. It is evident that GelMA/SFMA hydrogel was integrated throughout the gap of PCL scaffolds. Furthermore, spherical PM nanoparticles were uniformly dispersed throughout the hydrogel matrix. The successful loading of PTH within the MSNs and PM as well as homogeneous blending within the PM@GS/PCL were further validated by Fourier transform infrared spectrometer spectra, respectively (**Figure 3B**). The Fourier transform infrared spectrometer spectra of PM and PM@GS/PCL show that there are absorption peaks at 795 cm^{-1} due to the stretching vibration of the Si-O-Si bond. Additionally, thermogravimetric analysis was utilised to assess the PTH loading in PMs and PM embedding in PM@GS/PCL. After heating the nanoparticle powder, MSNs exhibited 88.18% residual mass, while PMs showed 84.96% weight loss, indicating the successful encapsulation of PTH within the MSNs and PMs blend in M@GS/PCL (**Figure 3C**). The mechanical curves of the composite scaffolds are displayed in **Additional Figure 1**. The compressive strength of PCL and GS/PCL scaffolds were 15.82 ± 0.60 and 17.81 ± 0.83 MPa, respectively (**Figure 3D**). The water contact angles of PCL and GS/PCL scaffolds measured were 96.6° and 71.9° respectively, which demonstrated the exceptional hydrophilicity of GS/PCL (**Figure 3E**). The improved hydrophilic property of the composite scaffolds can be attributed to the incorporation of hydrophilic GS hydrogel. Additionally, the *in vitro* release kinetics of PTH from both PMs and PM@GS/PCL were investigated (**Figure 3F**). From the release curves of PTH, it was observed that the release of PTH from the scaffold could last over a 21-day period. Obviously, the addition of PMs in PM@GS/PCL scaffold could reduce the release rate of PTH and would ensure the appropriate dose of PTH for biological stimulation.

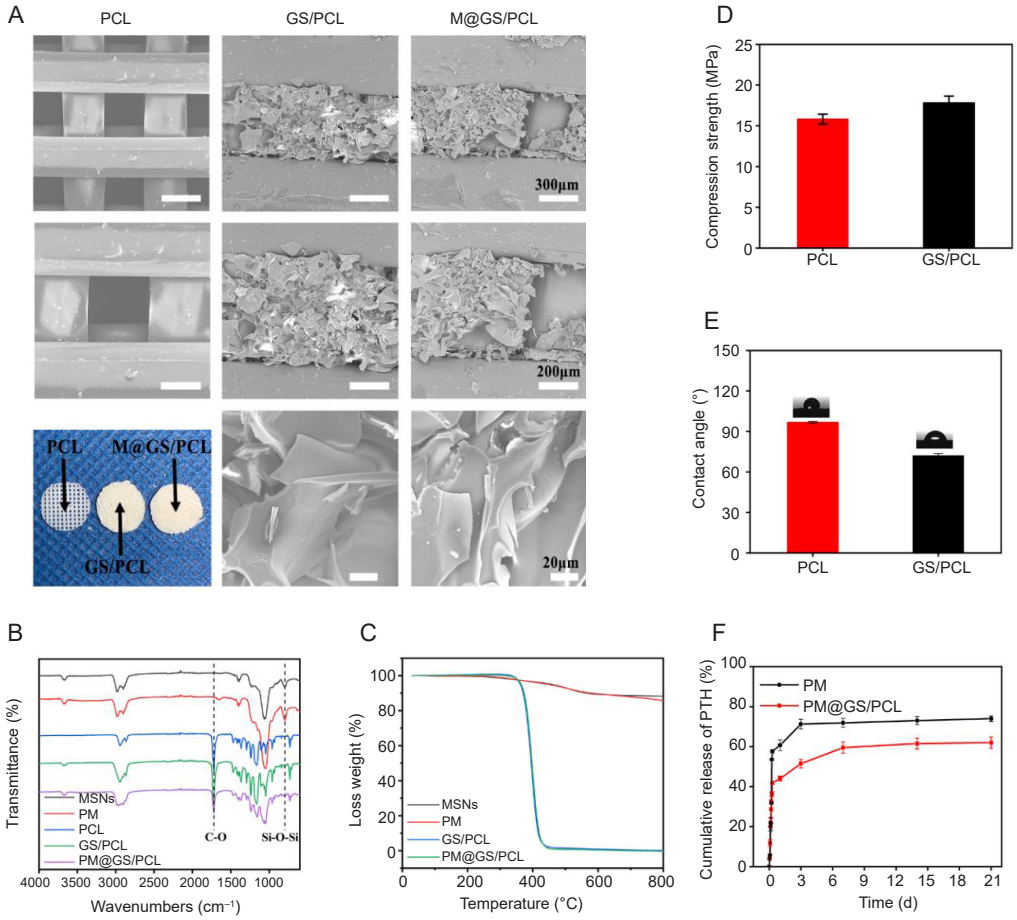

Figure 3. Characterisation of composite scaffolds. (A) SEM images of PCL, GS/PCL and M@GS/PCL at various magnifications and representative photographs of composite scaffolds. Scale bars: 300 μm (upper), 200 μm (middle) and 20 μm (lower). (B) ATR-FTIR spectra of MSNs and different composite scaffolds. (C) Thermogravimetric curves of MSNs, PTH@MSNs and different composite scaffolds. (D) Compressive strength of PCL and GS/PCL scaffolds. (E) Water contact angle of PCL and GS/PCL scaffolds. (F) The release curves of PTH from PTH@MSNs and PM@GS/PCL in PBS. Data in D–F are presented as the mean ± SD. ATR-FTIR: attenuated total reflectance-Fourier transform infrared; GelMA: methacrylate gelatin; GS: GelMA/SFMA composite hydrogel; M@GS/PCL: MSNs@GelMA/SFMA/PCL; MSNs: mesoporous silica nanoparticles; PBS: phosphate-buffered saline; PCL: polycaprolactone; PM: PTH@MSNs; PM@GS/PCL: PTH@MSNs/GelMA/SFMA/PCL; PTH: parathyroid hormone (1–34); SEM: scanning electron microscope; SFMA: methacrylated silk fibroin.

Biocompatibility and angiogenic activity of composite scaffolds

To study the biocompatibility of PCL, GS/PCL, M@GS/PCL, and PM@GS/PCL scaffolds, BMSCs were cultured on these scaffolds for 1, 3, and 5 days, and then evaluated using cell counting kit-8 and cellular staining assays. Furthermore, the proliferation and morphology of BMSCs on the scaffolds were examined with an inverted fluorescence microscope after Calcein-AM/PI staining. As depicted in the fluorescence images, the number of adhered cells on all scaffolds was significantly increased with prolonged culture time. (**Figure 4A**). On day 5, as compared to PCL and GS/PCL scaffolds, more cells were observed on PM@GS/PCL scaffold. Particularly remarkable was the ability of BMSCs to effectively penetrate the gaps within the scaffold, a notable accomplishment facilitated by the presence of GelMA/SFMA hydrogel embedded within the interstices of PCL filaments. Quantitative analysis of cells growth confirmed an obvious increase in BMSCs over time (**Figure 4B**). After 5 days of culture, the measured absorbance had risen approximately threefold compared to the initial measurement on day 1. Furthermore, while the optical densities of GS/PCL and M@GS/PCL groups were higher than that of PCL group, no significant difference in BMSCs proliferation can be observed between the GS/PCL and M@GS/PCL groups. These findings emphasize the supportive role of GelMA/SFMA hydrogel in promoting BMSCs proliferation. After the BMSCs internalised the nanoparticles, green fluorescence was observed from fluorescein isothiocyanate-labelled nanoparticles within the cytoplasm of BMSCs (**Additional Figure 2**).

To evaluate the *in vitro* recruitment capacity of the composite scaffolds, HUVECs underwent a Transwell migration assay. The results, shown in **Figure 4C**, demonstrate a compelling outcome. After 24 hours of culture, the PM@GS/PCL group

exhibited a substantial influx of HUVECs, whereas the other three groups showed minimal cell migration. This underscores the pronounced pro-recruitment effect of PTH released from the scaffolds on HUVECs migration. The angiogenic potential of the scaffolds was further assessed through an *in vitro* tube formation assay employing HUVECs. Following 6 and 24 hours of incubation, all groups exhibited varying degrees of tube formation (**Figure 4D**). The primary capillary-like networks were more pronounced after 24 hours of culture, while few tube-like structures were observed after 6 hours of incubation. Remarkably, the PM@GS/PCL group displayed a significantly superior tubular network formation compared to the GS/PCL and M@GS/PCL groups. Moreover, quantitative analysis using ImageJ software to measure total length, the number of junctions, the number of master segments, and the total master area per high-power field at 6 and 24 hours (**Figure 4E–H**) demonstrated obvious enhancement of all these parameters in the PM@GS/PCL group compared to the other groups. These results indicate that the PM@GS/PCL scaffold effectively releases PTH, guiding cellular migration and facilitating the formation of tubular structures. Moreover, PTH released from PM@GS/PCL can significantly improve angiogenic related genes (CD31 and VEGF) expression in HUVECs, suggesting that the release of PTH could induce angiogenesis (**Additional Figure 3**). Collectively, these results emphasize the exceptional proangiogenic potential of PTH-loaded scaffolds.

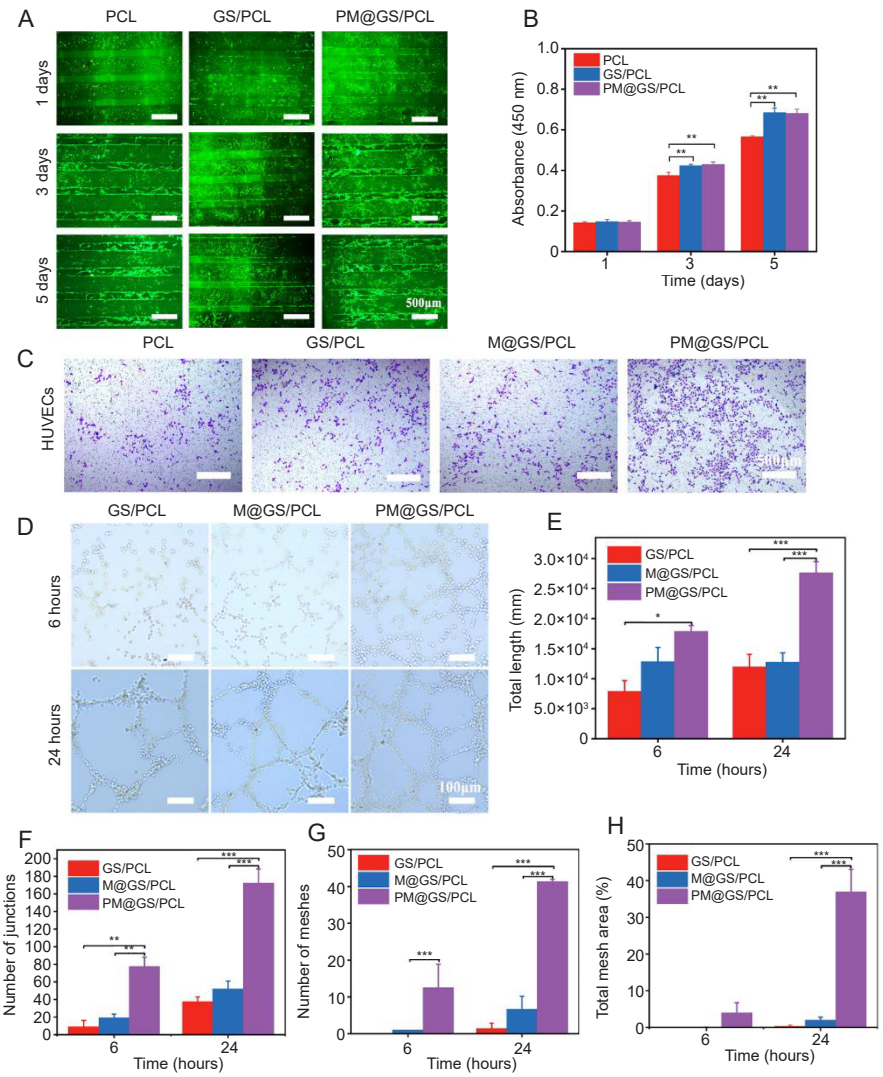

Figure 4. Impact of composite scaffolds on cell proliferation, migration and angiogenic activities. (A) BMSC proliferation on various scaffolds using a fluorescence microscope on days 1, 3 and 5. Viable cells were stained with Calcein-AM (green), while the dead cells were stained with PI (red). Scale bars: 500 μm. (B) Quantitative analysis of BMSCs proliferation with different scaffolds on days 1, 3 and 5 by CCK-8 assay. (C) Transwell migration assay for HUVECs at 24 hours using crystal violet staining. Scale bars: 500 μm. (D) Tube formation of HUVECs after 6 and 24 hours of incubation. Scale bars: 100 μm. (E–H) Quantitative assessment of angiogenic parameters, including total length, number of junctions, number of meshes, and total mesh area. Data are presented as the mean ± SD. $^{*}P < 0.05$, $^{**}P < 0.01$, $^{***}P < 0.001$ (one-way analysis of variance followed by Tukey's *post hoc* test). BMSC: bone marrow-derived mesenchymal stem cell; CCK-8: cell counting kit-8; GS/PCL: GelMA/SFMA/PCL; GelMA: methacrylate gelatin; HUVEC: human umbilical vein endothelial cell; M@GS/PCL: MSNs@GelMA/SFMA/PCL; MSNs: mesoporous silica nanoparticles; PCL: polycaprolactone; PI: propidium iodide; PM@GS/PCL: PTH@MSNs/GelMA/SFMA/PCL; PTH: parathyroid hormone (1–34); SFMA: methacrylated silk fibroin.

Osteogenic activities of composite scaffolds

The impact of these scaffolds on osteogenic differentiation of BMSCs was meticulously assessed through both quantitative and qualitative analyses using ALP and ARS staining. The ALP activity of BMSCs cultured with conditioned medium from various scaffolds is depicted in **Figure 5A**. There was color intensity on all scaffolds as the culture duration extended from day 7 to day 14. By day 14, a significant color intensity was observed on PM@GS/PCL scaffold group compared to other three groups. Compared with PCL and GS/PCL groups, the color intensities in the M@GS/PCL and PM@GS/PCL groups was significantly higher. Correspondingly, quantitative analysis corroborated these staining results, highlighting the robust ALP staining consistently observed in the PM@GS/PCL group at all time points (**Figure 5C**). Furthermore, after 14 and 21 days of induction, ARS staining of BMSCs was conducted (**Figure 5B**). Both optical and microscopic images displayed positive ARS staining outcomes across all groups. There was color intensity on all scaffolds as the culture duration extended form day 14 to day 21. However, significantly elevated mineralised nodules deposition was observed in the M@GS/PCL and PM@GS/PCL scaffolds groups on day 21, and PCL and GS/PCL scaffolds groups no significant differences. The highest level of mineralization, characterised by a quantitative analysis, was evident in the PM@GS/PCL group (**Figure 5D**). The effect of as-prepared scaffolds on osteogenic differentiation of BMSCs was investigated by measuring the osteogenesis-related genes expression using RT-PCR after 7 and 14 days of culture. As shown in **Figure 5E**, the level of *Runx2* expression in PM@GS/PCL group was higher than those of other groups. As displayed in **Figure 5F**, and **G**, the mRNA expression of downstream osteogenic markers *OCN* and *OPN* genes were also measured. It can be seen that the expression levels of *OCN* and *OPN* genes in the PM@GS/PCL group were significantly higher than those of other groups.

Radiographic assessment of bone regeneration in *in vivo* study

To thoroughly assess the *in vivo* osteogenic potential of different scaffolds, a 3 mm of diameter and depth in the rat femoral condyle defect, was created for implantation. As illustrated in **Figure 6A**, reconstructed micro-CT images of newly formed bone were captured at 4 weeks and 8 weeks of implantation. After 4 weeks, minimal new bone formation with larger defect areas, was evidently observed in the PCL scaffold and GS/PCL scaffold groups, the M@GS/PCL and PM@GS/PCL scaffold groups showed limited new bone formation at the defect sites. At 8 weeks post-implantation, the defect areas had diminished in all scaffold groups, accompanied by new bone formation along the implant outlines. Remarkably, the defect region in the PM@GS/PCL group had significantly contracted, displaying a substantial fusion of new bone along the defect rim, and it showed more new bone formation than PCL scaffold, M@GS/PCL scaffold and GS/PCL scaffold groups. The regenerated bone tissue area in the PM@GS/PCL group exceeded that in other groups, a phenomenon corroborated by sagittal sectional imaging. Furthermore, quantitative results of BMD, BV/TV and Tb. N revealed a significant enhancement in newly formed bone at the defect sites, particularly in groups implanted with scaffolds containing PTH (**Figure 6B–D**). The BV/TV of the PM@GS/PCL group reached 29.44 ± 4.12% at 8 weeks, which was notably higher than the M@GS/PCL (21.88 ± 1.88%), GS/PCL (19.57 ± 1.26%), and PCL (12.08 ± 2.21%) groups (**Figure 6C**).

Following micro-CT scanning, the promotive function of the composite scaffold on bone regeneration was further corroborated through histological examinations, which included haematoxylin and eosin and Masson's trichrome staining (**Figure** 7). Evaluation of haematoxylin and eosin-stained sections at 8 weeks post-implantation revealed no indications of malignancy, infection, or necrosis at implanted areas during the entire observation period. This finding highlights the excellent biocompatibility of the scaffolds. In the PCL scaffolds group, only a tiny amount of regenerated bone was found in the peripheral area near the original bone after 8 weeks. In contrast, a significant increase in newly formed bone tissue was noted in the injured sites following implantation with various composite scaffolds. In comparison to the PCL group, enhanced new bone formation was notably visible in the GS/PCL, M@GS/PCL, and PM@GS/PCL groups, particularly in the central regions of the defects. Remarkably, the PM@GS/PCL group displayed the most substantial bone formation, with newly regenerated bone almost filling the defect area. In parallel, Masson's trichrome staining results confirmed that PM@GS/PCL scaffolds induced extensive formation of new bone tissue within the bone defect area at the same site. Importantly, these histological findings underscored the synergistic osteogenic enhancement of MSNs and PTH *in vivo*. Consequently, the PM@GS/PCL scaffold emerged as the most effective promoter of bone regeneration.

Immunofluorescence staining was also performed to assess the expression of osteogenic markers (OPN and OCN) and the angiogenic marker (CD31) at the defect sites. As depicted in **Figure 8A**, minimal signals of osteogenic markers were monitored in the PCL and GS/PCL groups, with markedly weaker intensity than in the M@GS/PCL and PM@GS/PCL groups. Remarkably, the PM@GS/PCL group exhibited the highest levels of OPN and OCN expression (**Figure 8B**, and **C**). For the angiogenic evaluation, the CD31 expression was investigated at 8 weeks of implantation. The results revealed abundant CD31 expression in the repair site of the PM@GS/PCL group, indicating extensive neovascularisation. In contrast, the PCL group exhibited few new blood vessels, while the GS/PCL group displayed limited vascularisation (**Figure 8A**). Quantitative analysis of immunofluorescence intensity further confirmed significantly elevated CD31 expression in the PM@GS/PCL group compared to other groups (**Figure 8D**). The PM@GS/PCL scaffold demonstrated exceptional biocompatibility, enhanced osteogenic and angiogenic potential, and efficient bone defect healing ability. These results suggest that the structurally and functionally optimised PM@GS/PCL scaffold was suitable for applications in bone defect repair.

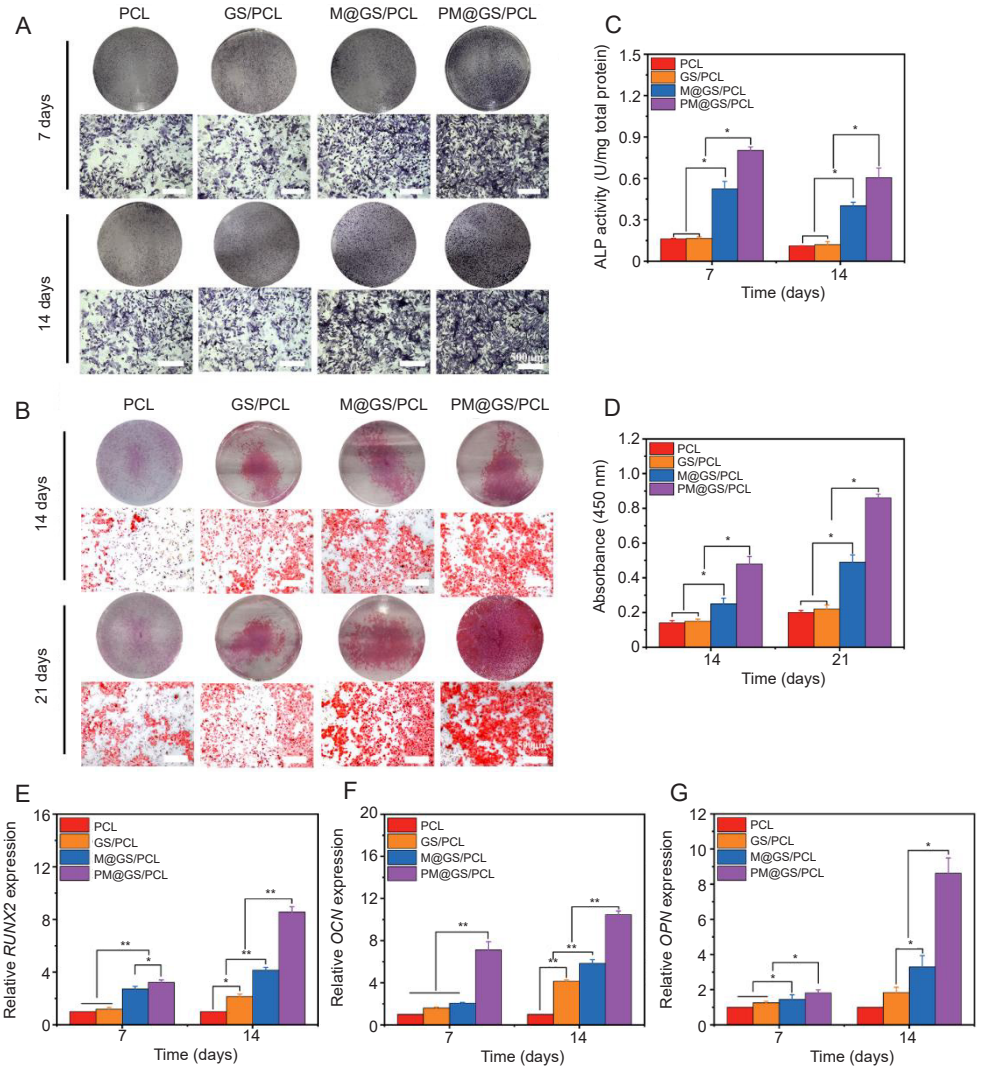

Figure 5. *In vitro* osteogenic potential of scaffold extracts. (A) Representative images of ALP staining of BMSCs cultured with the conditioned medium from different scaffolds on days 7 and 14. Scale bars: 500 μm. (B) Representative images of ARS staining of BMSCs cultured with extracts from different scaffolds to observe the mineral matrix formation on days 14 and 21. Scale bars: 500 μm. (C) Quantitative result of ALP activity on days 7 and 14. (D) Quantitative result of ARS on days 14 and 21. (E–G) Expression of osteogenesis-related genes in BMSCs after incubation with different scaffold extracts for 7 and 14 days, including *Runx2* (E), *OCN* (F), and *OPN* (G). Data are presented as the mean ± SD. $^{*}P < 0.05$, $^{**}P < 0.01$ (one-way analysis of variance followed by Tukey's *post hoc* test). ALP: alkaline phosphatase; ARS: Alizarin red S; BMSC: bone marrow-derived mesenchymal stem cell; GS/PCL: GelMA/SFMA/PCL; GelMA: methacrylate gelatin; M@GS/PCL: MSNs@GelMA/SFMA/PCL; MSNs: mesoporous silica nanoparticles; OCN: osteocalcin; OPN: osteopontin; PCL: polycaprolactone; PM@GS/PCL: PTH@MSNs/GelMA/SFMA/PCL; PTH: parathyroid hormone (1–34); Runx2: runt-related transcription factor 2; SFMA: methacrylated silk fibroin.

Discussion

PCL is widely employed in bone scaffolds due to its favourable attributes such as low immunogenicity and suitable degradation properties.[43] However, despite its utility, PCL exhibits limitations such as restricted biocompatibility and inadequate cell adhesion. To address these shortcomings, we hypothesised that incorporating GelMA/SFMA into PCL scaffolds could enhance their biocompatibility for implantation application. To achieve a biomimetic scaffold, we established a hierarchical structure by infusing porous hydrogel into the gaps of 3D-printed scaffolds to create a supportive framework. The successful preparation of MSNs was confirmed through transmission electron microscope and scanning electron microscope analyses. Additionally, DLS and zeta potential measurements verified the effective loading of PTH into the MSNs. GelMA/SFMA hydrogel and PMs/GS hydrogel were integrated throughout the gaps of PCL scaffolds to produce GS/PCL and M@GS/PCL scaffolds. In M@GS/PCL scaffolds, spherical MSNs were uniformly dispersed within the GelMA/SFMA hydrogel matrix. Previous studies have indicated that an optimal level of roughness on pore walls promotes cell adhesion and migration.[44, 45] Fourier transform infrared spectrometre spectra and thermogravimetric analysis further confirmed the successful loading of PTH into the MSNs and the presence

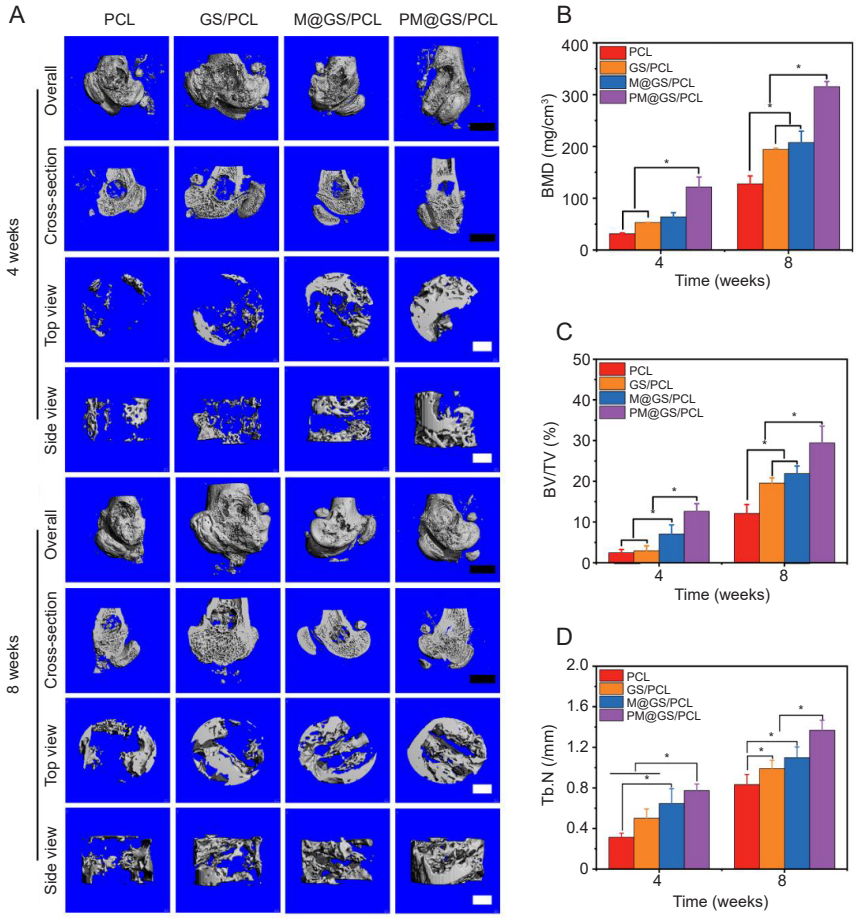

Figure 6. Bone regeneration in rat femoral condyle defect model with a diameter of 3 mm. (A) 3D reconstructed micro-CT images after scaffold implantation for 4 and 8 weeks, including overall, cross-section, top view and side view. Black scale bars: 1 mm; white scale bars: 500 μm. (B) BMD, (C) BV/TV and (D) Tb. N analysis of newly formed bone tissues obtained from micro-CT results. Data are presented as the mean ± SD. *$P < 0.05$ (one-way analysis of variance followed by Tukey's *post hoc* test). 3D: three-dimensional; BMD: bone mineral density; BV/TV: ratio of new bone volume to total volume; CT: computed tomography; GS/PCL: GelMA/SFMA/PCL; GelMA: methacrylate gelatin; M@GS/PCL: MSNs@GelMA/SFMA/PCL; MSNs: mesoporous silica nanoparticles; PCL: polycaprolactone; PM@GS/PCL: PTH@MSNs/GelMA/SFMA/PCL; PTH: parathyroid hormone (1–34); SFMA: methacrylated silk fibroin; Tb. N: trabecular number.

of GelMA/SFMA hydrogel within the PCL scaffolds. The *in vitro* release kinetics of PTH from both PM and PM@GS/PCL revealed continuous release from the MSNs, with a slower release rate observed from the PM@GS/PCL scaffold. This release pattern is likely attributed to the gradual degradation of the scaffold, resulting in the prolonged release of PTH into the surrounding medium.

The biocompatibility of PCL, GS/PCL, M@GS/PCL, and PM@GS/PCL scaffolds was assessed through BMSCs proliferation and cellular staining assays. Both quantitative and qualitative analyses revealed a noticeable increase in BMSCs proliferation across all scaffold types, with a particularly significant increase observed in the PM@GS/PCL scaffold group. These findings underscore the good biocompatibility of PM@GS/PCL scaffolds. Endothelial cell recruitment is pivotal for new blood vessel formation, crucial for expediting bone reconstruction during the repair process.[46] To assess the angiogenic potential of the scaffolds, transwell migration assay and *in vitro* tube formation assay were performed. The transwell migration assay demonstrated maximal HUVECs migration in the PM@GS/PCL scaffold group, while quantitative and qualitative analyses of the tube formation assay indicated enhanced tube formation in the PM@GS/PCL scaffold group. These results align with previous studies highlighting the beneficial effects of PTH in endothelial cell recruitment and osteogenic activity.[33] *In vitro* assessments of osteogenic differentiation were conducted using ALP staining and ARS staining of BMSCs. The intensity of staining increased on all scaffolds with extended culture duration, with significantly amplified color intensity observed in the PM@GS/PCL scaffold group. Quantitative analysis corroborated these staining results. Additionally, osteogenesis-related genes expression analysis revealed higher expression levels of *Runx2*, *OCN*, and *OPN* genes in the PM@GS/PCL group compared to other groups. Taken together, these findings support the conclusion that the PM@GS/PCL scaffold significantly enhances osteogenic differentiation and accelerates the formation of mineralised matrices.

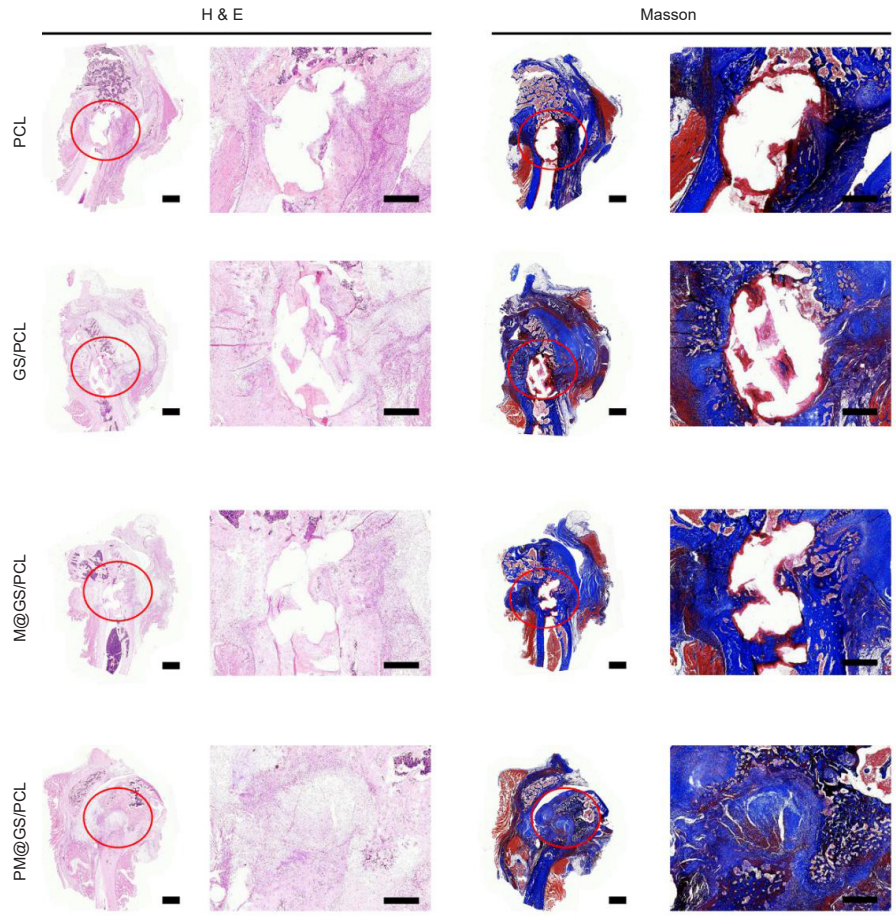

Figure 7. Histological analysis of femoral condyle defect at 8 weeks including H&E staining and Masson's trichrome staining. Red circles indicate the areas of bone defect. Scale bars: 1 mm. GS/PCL: GelMA/SFMA/PCL; GelMA: methacrylate gelatin; H&E: haematoxylin and eosin; M@GS/PCL: MSNs@GelMA/SFMA/PCL; MSNs: mesoporous silica nanoparticles; PCL: polycaprolactone; PM@GS/PCL: PTH@MSNs/GelMA/SFMA/PCL; PTH: parathyroid hormone (1–34); SFMA: methacrylated silk fibroin.

From the 3D reconstructed micro-CT images, it demonstrated that PM@GS/PCL scaffold groups exhibited a large amount of newly formed bone tissue. Correspondingly, quantitative analysis of BMD, BV/TV and Tb. N also corroborated these micro-CT images results. Bone-regenerative potential was further corroborated through histological examinations. The sections of different group scaffolds revealed no indications of malignancy, infection, or necrosis, and demonstrated they had excellent biocompatibility. Moreover, the results of histological staining also corroborated micro-CT results. This finding indicates that the presence of PTH significantly promoted *in vivo* new bone formation. Additionally, BMD measurements and Tb. N analysis was consistent with BV/TV and histological examinations, further emphasizing the superior bone regeneration effect of PM@GS/PCL scaffold. Furthermore, immunofluorescence staining of osteogenesis-related markers (OPN and OCN) and the angiogenic marker (CD31) at the defect sites was used to assess osteogenic and angiogenic performance. These results revealed abundant CD31, OPN and OCN expression in the repair site of the PM@GS/PCL group. Previous studies have demonstrated PTH's ability to induce elevated CD31 expression in HUVECs, thereby enhancing early vascularisation, which subsequently promotes vascularisation and new bone formation during bone repair.[47] Our results indicate that the structurally and functionally optimised PM@GS/PCL scaffold was suitable for applications in bone defect repair. In this study, the process for the fabrication of PM@GS/PCL composite scaffold is relatively complicated. Moving forward, we envision simplifying the fabrication process through the utilization of a dual-axis bioprinter, aiming to achieve enhanced efficiency and scalability.

In summary, we have successfully fabricated a PM@GS/PCL composite scaffold tailored for bone defect repair. Through the infusion of the 3D-printed PCL framework with a GelMA/SFMA hydrogel matrix loaded with PM, a sophisticated 3D architecture was achieved. The incorporation of PM in scaffold is to stimulate angiogenic and osteogenic processes for bone regeneration. This collaborative arrangement of PCL filaments and GelMA/SFMA hydrogel matrix established a hierarchical structure, offering an ideal environment for cellular attachment and proliferation. Importantly, this composite scaffold exhibited remarkable compressive strength, a result of the synergistic integration of the 3D-printed PCL framework and

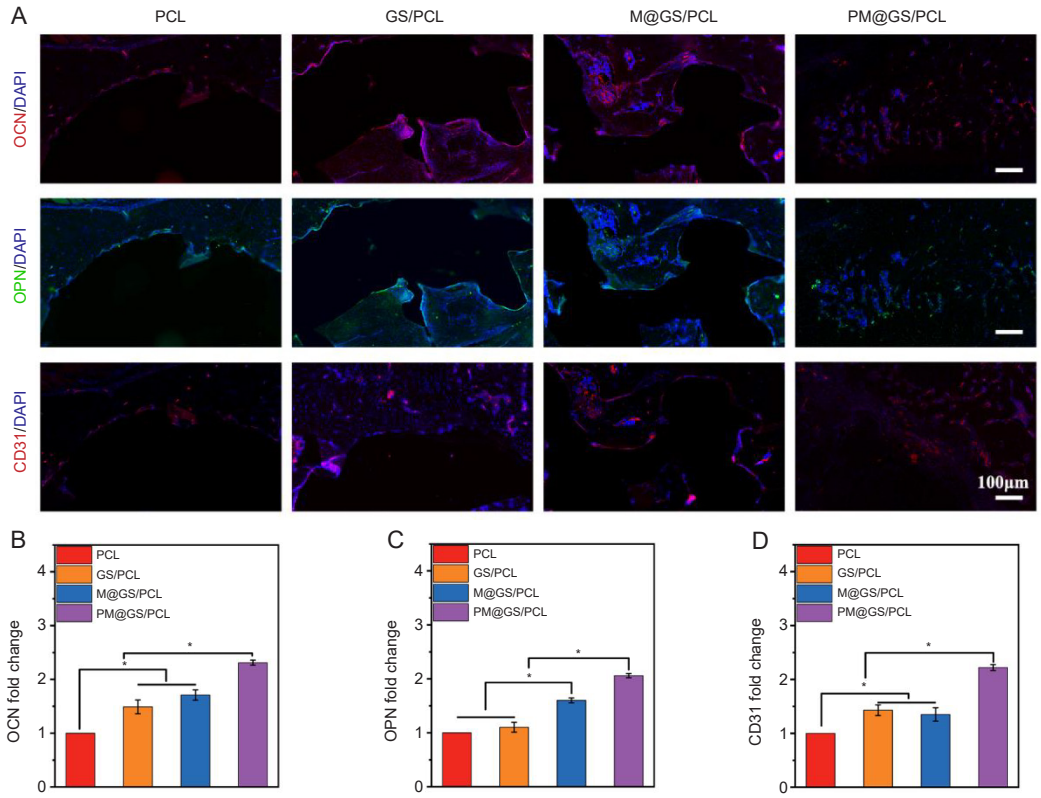

Figure 8. Assessment of osteogenic potential of various scaffolds using immunofluorescence staining. (A) Fluorescence images of OCN (red), OPN (green), and CD31 (red) after implantation for 8 weeks. The nuclei were stained with DAPI (blue). (B–D) Quantification of OCN, OPN and CD31 expression. Data are presented as the mean ± SD (one-way analysis of variance followed by Tukey's *post hoc* test). *P < 0.05. CD31: platelet endothelial cell adhesion molecule-1; DAPI: 4′,6-diamidino-2-phenylindole; GS/PCL: GelMA/SFMA/PCL; GelMA: methacrylate gelatin; M@GS/PCL: MSNs@GelMA/SFMA/PCL; MSNs: mesoporous silica nanoparticles; OCN: osteocalcin; OPN: osteopontin; PCL: polycaprolactone; PM@GS/PCL: PTH@MSNs/GelMA/SFMA/PCL; PTH: parathyroid hormone (1–34); SFMA: methacrylated silk fibroin.

GelMA/SFMA hydrogel. Significantly, the scaffold not only offered an extracellular matrix-mimicking 3D environment but also efficiently delivered PTH, orchestrating simultaneous osteogenesis and angiogenesis. Our *in vitro* investigations unequivocally affirmed the scaffold's capacity to support cell proliferation, expedite HUVECs' migration, and enhance angiogenic and osteogenic potentials. More significantly, when implanted into rat femoral condyle defects, the PM@GS/PCL scaffold significantly accelerated bone regeneration. The scaffold's superior microstructure and sustained PTH release played a pivotal role in driving both angiogenesis and osteogenesis, culminating in exceptional regenerative outcomes. In conclusion, this 3D printed composite scaffold in our study has the potential to guide rapid vascularised bone regeneration, offering a new alternative for bone defect treatment.

Author contributions

JY: Investigation, methodology, data curation, writing original draft; KF: writing – review & editing; XZ: conceptualization, writing – review & editing; CH: conceptualization, supervision, project administration, funding acquisition, writing – review & editing. All authors approved the final version of the manuscript.

Financial support

This study was supported by the National Natural Science Foundation of China (Nos. 32071350, 32171404), Fundamental Research Funds for the Central Universities (No. 2232019A3-06), International Cooperation Fund of the Science and Technology Commission of Shanghai Municipality (No. 19440741600), Natural Science Foundation of Shanghai (No. 21ZR1403100), Science and Technology Commission of Shanghai Municipality (No. 20DZ2254900) and Biomaterials and Regenerative Medicine Institute Cooperative Research Project by Shanghai Jiao Tong University School of Medicine (No. 2022LHB03).

Acknowledgement

None.

Conflicts of interest statement

The authors declare that they have no known competing financial interests or personal relationships that could have appeared to influence the work reported in this paper.

Additional files

Additional Figure 1: Compressive stress–strain curve of PCL and GS/PCL scaffolds.

Additional Figure 2: Confocal microscopy images of BMSCs treated with MSNs (A) and fluorescein isothiocyanate-labelled MSNs (green; B) for 48 hours.

Additional Figure 3: Effect of different scaffold extracts on the expression of angiogenesis-related genes in HUVECs at 48 hours.

Additional Table 1: Primers for real-time polymerase chain reaction analysis in BMSCs and HUVECs.

1. Hao, S.; Wang, M.; Yin, Z.; Jing, Y.; Bai, L.; Su, J. Microenvironment-targeted strategy steers advanced bone regeneration. *Mater Today Bio.* **2023**, *22*, 100741.
2. Ma, H.; Yang, C.; Ma, Z.; Wei, X.; Younis, M. R.; Wang, H.; Li, W.; Wang, Z.; Wang, W.; Luo, Y.; Huang, P.; Wang, J. Multiscale hierarchical architecture-based bioactive scaffolds for versatile tissue engineering. *Adv Healthc Mater.* **2022**, *11*, e2102837.
3. Wang, W.; Yeung, K. W. K. Bone grafts and biomaterials substitutes for bone defect repair: A review. *Bioact Mater.* **2017**, *2*, 224-247.
4. Spetzger, U.; Vougioukas, V.; Schipper, J. Materials and techniques for osseous skull reconstruction. *Minim Invasive Ther Allied Technol.* **2010**, *19*, 110-121.
5. Yang, Y.; Wang, X.; Qian, H.; Cheng, L. Titanium-based sonosensitizers for sonodynamic cancer therapy. *Appl Mater Today.* **2021**, *25*, 101215.
6. Sedghi, R.; Shaabani, A.; Sayyari, N. Electrospun triazole-based chitosan nanofibers as a novel scaffolds for bone tissue repair and regeneration. *Carbohydr Polym.* **2020**, *230*, 115707.
7. Dong, J.; Li, Y.; Lin, P.; Leeflang, M. A.; van Asperen, S.; Yu, K.; Tümer, N.; Norder, B.; Zadpoor, A. A.; Zhou, J. Solvent-cast 3D printing of magnesium scaffolds. *Acta Biomater.* **2020**, *114*, 497-514.
8. Tang, Y.; Lin, S.; Yin, S.; Jiang, F.; Zhou, M.; Yang, G.; Sun, N.; Zhang, W.; Jiang, X. In situ gas foaming based on magnesium particle degradation: a novel approach to fabricate injectable macroporous hydrogels. *Biomaterials.* **2020**, *232*, 119727.
9. Shahbazarab, Z.; Teimouri, A.; Chermahini, A. N.; Azadi, M. Fabrication and characterization of nanobiocomposite scaffold of zein/chitosan/nanohydroxyapatite prepared by freeze-drying method for bone tissue engineering. *Int J Biol Macromol.* **2018**, *108*, 1017-1027.
10. Jian, Z.; Zhuang, T.; Qinyu, T.; Liqing, P.; Kun, L.; Xujiang, L.; Diaodiao, W.; Zhen, Y.; Shuangpeng, J.; Xiang, S.; Jingxiang, H.; Shuyun, L.; Libo, H.; Peifu, T.; Qi, Y.; Quanyi, G. 3D bioprinting of a biomimetic meniscal scaffold for application in tissue engineering. *Bioact Mater.* **2021**, *6*, 1711-1726.
11. Ligon, S. C.; Liska, R.; Stampfl, J.; Gurr, M.; Mülhaupt, R. Polymers for 3D printing and customized additive manufacturing. *Chem Rev.* **2017**, *117*, 10212-10290.
12. Ali, M. A.; Hu, C.; Yttri, E. A.; Panat, R. Recent advances in 3D printing of biomedical sensing devices. *Adv Funct Mater.* **2022**, *32*, 2107671.
13. Feng, Y.; Zhu, S.; Mei, D.; Li, J.; Zhang, J.; Yang, S.; Guan, S. Application of 3D printing technology in bone tissue engineering: a review. *Curr Drug Deliv.* **2021**, *18*, 847-861.
14. Kong, B.; Zhao, Y. 3D bioprinting for biomedical applications. *BME Front.* **2023**, *4*, 0010.
15. Dai, X.; Shao, Y.; Tian, X.; Cao, X.; Ye, L.; Gao, P.; Cheng, H.; Wang, X. Fusion between glioma stem cells and mesenchymal stem cells promotes malignant progression in 3D-bioprinted models. *ACS Appl Mater Interfaces.* **2022**, *14*, 35344-35356.
16. Gao, X.; Xu, Z.; Liu, G.; Wu, J. Polyphenols as a versatile component in tissue engineering. *Acta Biomater.* **2021**, *119*, 57-74.
17. Ojha, A. K.; Rajasekaran, R.; Hansda, A. K.; Singh, A.; Dutta, A.; Seesala, V. S.; Das, S.; Dogra, N.; Sharma, S.; Goswami, R.; Chaudhury, K.; Dhara, S. Biodegradable multi-layered silk fibroin-PCL stent for the management of cervical atresia: in vitro cytocompatibility and extracellular matrix remodeling in vivo. *ACS Appl Mater Interfaces.* **2023**, *15*, 39099-39116.
18. Yang, X.; Wang, Y.; Zhou, Y.; Chen, J.; Wan, Q. The application of polycaprolactone in three-dimensional printing scaffolds for bone tissue engineering. *Polymers (Basel).* **2021**, *13*, 2754.
19. Neufurth, M.; Wang, X.; Wang, S.; Steffen, R.; Ackermann, M.; Haep, N. D.; Schröder, H. C.; Müller, W. E. G. 3D printing of hybrid biomaterials for bone tissue engineering: Calcium-polyphosphate microparticles encapsulated by polycaprolactone. *Acta Biomater.* **2017**, *64*, 377-388.
20. Rodríguez-Merchán, E. C. Bone healing materials in the treatment of recalcitrant nonunions and bone defects. *Int J Mol Sci.* **2022**, *23*, 3352.
21. Nitzsche, B.; Rong, W. W.; Goede, A.; Hoffmann, B.; Scarpa, F.; Kuebler, W. M.; Secomb, T. W.; Pries, A. R. Coalescent angiogenesis-evidence for a novel concept of vascular network maturation. *Angiogenesis.* **2022**, *25*, 35-45.
22. Koushik, T. M.; Miller, C. M.; Antunes, E. Bone tissue engineering scaffolds: function of multi-material hierarchically structured scaffolds. *Adv Healthc Mater.* **2023**, *12*, e2202766.
23. Xiong, Y.; Mi, B. B.; Lin, Z.; Hu, Y. Q.; Yu, L.; Zha, K. K.; Panayi, A. C.; Yu, T.; Chen, L.; Liu, Z. P.; Patel, A.; Feng, Q.; Zhou, S. H.; Liu, G. H. The role of the immune microenvironment in bone, cartilage, and soft tissue regeneration: from mechanism to therapeutic opportunity. *Mil Med Res.* **2022**, *9*, 65.
24. Xu, Y.; Xu, C.; He, L.; Zhou, J.; Chen, T.; Ouyang, L.; Guo, X.; Qu, Y.; Luo, Z.; Duan, D. Stratified-structural hydrogel incorporated with magnesium-ion-modified black phosphorus nanosheets for promoting neuro-vascularized bone regeneration. *Bioact Mater.* **2022**, *16*, 271-284.
25. Marrella, A.; Lee, T. Y.; Lee, D. H.; Karuthedom, S.; Syla, D.; Chawla, A.; Khademhosseini, A.; Jang, H. L. Engineering vascularized and innervated bone biomaterials for improved skeletal tissue regeneration. *Mater Today (Kidlington).* **2018**, *21*, 362-376.
26. Huang, B.; Chen, M.; Tian, J.; Zhang, Y.; Dai, Z.; Li, J.; Zhang, W. Oxygen-carrying and antibacterial fluorinated nano-hydroxyapatite incorporated hydrogels for enhanced bone regeneration. *Adv Healthc Mater.* **2022**, *11*, e2102540.
27. Carmeliet, P. Angiogenesis in health and disease. *Nat Med.* **2003**, *9*, 653-660.
28. Wang, J.; Wang, H.; Wang, Y.; Liu, Z.; Li, Z.; Li, J.; Chen, Q.; Meng, Q.; Shu, W. W.; Wu, J.; Xiao, C.; Han, F.; Li, B. Endothelialized microvessels fabricated by microfluidics facilitate osteogenic differentiation and promote bone repair. *Acta Biomater.* **2022**, *142*, 85-98.
29. Gong, L.; Yang, Z.; Zhang, F.; Gao, W. Cytokine conjugates to elastin-like polypeptides. *Adv Drug Deliv Rev.* **2022**, *190*, 114541.
30. Paschold, A.; Voigt, B.; Hause, G.; Kohlmann, T.; Rothemund, S.; Binder, W. H. Modulating the fibrillization of parathyroid-hormone (PTH) peptides: azo-switches as reversible and catalytic entities. *Biomedicines.* **2022**, *10*, 1512.
31. Martin, T. J.; Sims, N. A.; Seeman, E. Physiological and pharmacological roles of PTH and PTHrP in bone using their shared receptor, PTH1R. *Endocr Rev.* **2021**, *42*, 383-406.
32. Huang, J.; Lin, D.; Wei, Z.; Li, Q.; Zheng, J.; Zheng, Q.; Cai, L.; Li, X.; Yuan, Y.; Li, J. Parathyroid hormone derivative with reduced osteoclastic activity promoted bone regeneration via synergistic bone remodeling and angiogenesis. *Small.* **2020**, *16*, e1905876.
33. Jiang, L.; Zhang, W.; Wei, L.; Zhou, Q.; Yang, G.; Qian, N.; Tang, Y.; Gao, Y.; Jiang, X. Early effects of parathyroid hormone on vascularized bone regeneration and implant osseointegration in aged rats. *Biomaterials.* **2018**, *179*, 15-28.
34. Liu, S.; Han, Z.; Hao, J. N.; Zhang, D.; Li, X.; Cao, Y.; Huang, J.; Li, Y.

Engineering of a NIR-activable hydrogel-coated mesoporous bioactive glass scaffold with dual-mode parathyroid hormone derivative release property for angiogenesis and bone regeneration. *Bioact Mater.* **2023**, *26*, 1-13.
35. Zhao, Y.; Kang, H.; Wu, X.; Zhuang, P.; Tu, R.; Goto, T.; Li, F.; Dai, H. Multifunctional scaffold for osteoporotic pathophysiological microenvironment improvement and vascularized bone defect regeneration. *Adv Healthc Mater.* **2023**, *12*, e2203099.
36. Mirkhalaf, M.; Men, Y.; Wang, R.; No, Y.; Zreiqat, H. Personalized 3D printed bone scaffolds: A review. *Acta Biomater.* **2023**, *156*, 110-124.
37. Hull, S. M.; Brunel, L. G.; Heilshorn, S. C. 3D bioprinting of cell-laden hydrogels for improved biological functionality. *Adv Mater.* **2022**, *34*, e2103691.
38. Sun, L.; Wang, X.; Gong, F.; Yin, K.; Zhu, W.; Yang, N.; Bai, S.; Liao, F.; Shao, M.; Cheng, L. Silicon nanowires decorated with platinum nanoparticles were applied for photothermal-enhanced sonodynamic therapy. *Theranostics.* **2021**, *11*, 9234-9242.
39. Sun, P.; Zhang, Q.; Nie, W.; Zhou, X.; Chen, L.; Du, H.; Yang, S.; You, Z.; He, J.; He, C. Biodegradable mesoporous silica nanocarrier bearing angiogenic QK peptide and dexamethasone for accelerating angiogenesis in bone regeneration. *ACS Biomater Sci Eng.* **2019**, *5*, 6766-6778.
40. Yang, J.; Li, Z.; Li, S.; Zhang, Q.; Zhou, X.; He, C. Tunable metacrylated silk fibroin-based hybrid bioinks for the bioprinting of tissue engineering scaffolds. *Biomater Sci.* **2023**, *11*, 1895-1909.
41. Li, Z.; Li, S.; Yang, J.; Ha, Y.; Zhang, Q.; Zhou, X.; He, C. 3D bioprinted gelatin/gellan gum-based scaffold with double-crosslinking network for vascularized bone regeneration. *Carbohydr Polym.* **2022**, *290*, 119469.
42. Schneider, C. A.; Rasband, W. S.; Eliceiri, K. W. NIH image to ImageJ: 25 years of image analysis. *Nat Methods.* **2012**, *9*, 671-675.
43. Zhou, X.; Liu, P.; Nie, W.; Peng, C.; Li, T.; Qiang, L.; He, C.; Wang, J. Incorporation of dexamethasone-loaded mesoporous silica nanoparticles into mineralized porous biocomposite scaffolds for improving osteogenic activity. *Int J Biol Macromol.* **2020**, *149*, 116-126.
44. Mora-Raimundo, P.; Lozano, D.; Benito, M.; Mulero, F.; Manzano, M.; Vallet-Regí, M. Osteoporosis remission and new bone formation with mesoporous silica nanoparticles. *Adv Sci (Weinh).* **2021**, *8*, e2101107.
45. Woodruff, M. A.; Hutmacher, D. W. The return of a forgotten polymer—Polycaprolactone in the 21st century. *Prog Polym Sci.* **2010**, *35*, 1217-1256.
46. Liang, K.; Zhao, C.; Song, C.; Zhao, L.; Qiu, P.; Wang, S.; Zhu, J.; Gong, Z.; Liu, Z.; Tang, R.; Fang, X.; Zhao, Y. In situ biomimetic mineralization of bone-like hydroxyapatite in hydrogel for the acceleration of bone regeneration. *ACS Appl Mater Interfaces.* **2023**, *15*, 292-308.
47. Vadana, M.; Cecoltan, S.; Ciortan, L.; Macarie, R. D.; Mihaila, A. C.; Tucureanu, M. M.; Gan, A. M.; Simionescu, M.; Manduteanu, I.; Droc, I.; Butoi, E. Parathyroid hormone induces human valvular endothelial cells dysfunction that impacts the osteogenic phenotype of valvular interstitial cells. *Int J Mol Sci.* **2022**, *23*, 3776.

Received: December 6, 2023
Revised: February 8, 2024
Accepted: February 29, 2024
Available online: March 28, 2024